Absolute Differential Elastic- and Inelastic-Scattering Cross Sections in 25–140 keV He^+ + He Collisions*

Victor Pol, Walter Kauppila,† and John T. Park
Physics Department, University of Missouri-Rolla, Rolla, Missouri 65401
(Received 13 July 1973)

Data obtained as energy-loss spectra at angles from 0 to 7.3×10^{-3} rad (c.m.) with typical energy-loss resolution of 0.7 eV and angular resolution of 2×10^{-3} rad (c.m.) were used to calculate average differential cross sections $\langle d\sigma/d\Omega\rangle_{av}$ for elastic scattering, direct excitation of the individual He($n=2$) states, and direct excitation of the $He^+(n=2)$ states. The total cross section for excitation of the He($n=2$) states obtained by integrating the differential cross sections was found to be 20×10^{-18} cm^2 at 25 keV (lab) decreasing to 7×10^{-18} cm^2 at 140 keV. At incident lab energies below 100 keV the He($2\,^3S$) and He($2\,^3P$) states dominate the He($n=2$) structure at angles close to zero, while the He($2\,^1P$) state dominates at larger angles. The contribution of the He($2\,^1S$) state remains below 25% at all angles and energies.

I. INTRODUCTION

Helium-ion–helium-atom collisions have received a great deal of interest because helium is particularly well suited for experimental purposes. In the 25–140-keV energy range, studies of direct excitation processes have been limited to optical measurements of radiation for the collisionally excited states. Previous optical studies of emission-cross-section measurements have been extensively reviewed by Thomas[1] and, to our knowledge, have involved states with $n\geq3$. Except for our previous measurements,[2,3] no results are available on direct excitation of the He($n=2$) or the $He^+(n=2)$ states in He^+ + He collisions at energies above the 3 keV.

The present experiment is designed to study the angular scattering in the collision processes:

$$\begin{aligned} He^+(1s)+He(1s^2) &\rightarrow He^+(1s)+He(1s^2)\\ &\rightarrow He^+(1s)+He(1s2l)\\ &\rightarrow He^+(n=2)+He(1s^2)\ . \end{aligned}$$

The experiment is a logical extension of our previous work, in which only particles scattered in the forward direction were detected and total cross sections were calculated from the data by assuming that we could neglect particles scattered through angles greater than the acceptance angle of the detector. By measuring the angular dependence of the scattered ions we not only investigate the validity of the above assumption, but we also provide a strong test of theoretical calculations in this energy range. Furthermore, several interesting features show up in comparing our results with those of angular-scattering measurements at lower energies, which might lead to new applications of existing models or to more reliable models for collision processes in this energy range.

II. EXPERIMENTAL

Over-all Apparatus

The energy-loss spectrometer at the University of Missouri-Rolla and the general method employed in heavy-ion energy-loss spectrometry have been discussed in detail elsewhere.[4–6] Several changes were incorporated into the apparatus to make accurate angular measurements possible. A schematic of the apparatus is shown in Fig. 1. In the current experiment, ions produced in a low-voltage discharge source are focused and mass analyzed by a Wien filter. Mass-selected ions are then accelerated and steered through a variable-angle collimator into a target chamber containing the gas under study. After traversing the scattering chamber, the ions pass through an exit collimator and the transmitted beam is magnetically analyzed to remove any products of charge-changing collisions. Following the magnet a set of movable slits may be positioned accurately in both the vertical and horizontal planes to assist in measuring the acceptance angle of the deceleration-column–energy-analyzer system. Ions entering the decelerator are decelerated by a well-defined potential and analyzed by a 127° electrostatic energy analyzer.

Spectra differential in energy loss are obtained by increasing ΔV, the potential between the accelerator and decelerator terminals. Whenever the increased potential energy compensates for a discrete energy loss of the projectile-target system, a peak is detected in the spectrum. The energy-loss scale can be determined to an accu-

racy of ±0.03 eV.[6]

When measurements differential in scattering angle are made, the basic technique is as discussed above except that a series of measurements are made with different incident-ion beam angles. Figure 2 presents the details of the apparatus used for angular measurements. The angle at which the beam enters the target chamber can be varied by changing the entrance collimator angle θ and adjusting the voltage on two pairs of vertical deflection plates which precede the collimator.

The systematic errors involved in making angular measurements have been discussed in detail by others for various geometries and different angular ranges.[7-12] Our experiment is arranged such that variations in the length of the interaction region with scattering angle are negligible or can be calculated. Also, because of the small angles at which we are working, the change in the acceptance angle of the detector with scattering angle is less than 1%. Working at very small angles, however, maximizes the errors due to uncertainty in the scattering angle which result from the finite sizes of the apertures.

Analysis of Angular Factors

The locations and dimensions of our apertures are given in Fig. 3. (In the following discussion all quantities, such as divergence of the beam and angular acceptance of the detector, are given in lab coordinates, whereas the data in Sec. III are given for center-of-mass angles.) The interaction region is determined by the intersection of the beam with the interior of the collision cell. If every particle which goes through aperture f were detected, the average acceptance angle would be 8.7×10^{-4} rad in both the vertical and horizontal planes and would not change with the angle of the incident beam. The true acceptance angles, however, are also dependent on the entrance slits in the energy analyzer and the focusing effects of the deceleration column. We were able to determine the detection efficiency across the effective window of the decelerator-analyzer system by moving slits h and g across the front of the deceleration column and measuring the current in both the analyzer and in a cup directly behind the slits as a function of the position of these slits. The vertical acceptance angle of the decelerator-analyzer system, calculated in this way, varied from 0.5×10^{-4} to 5×10^{-4} rad, and the horizontal acceptance angle varied from 2×10^{-4} to 7×10^{-4} rad depending on deceleration voltage. (The horizontal acceptance angle was wider than the vertical acceptance because the entrance slits in the analyzer are horizontal.) Thus in all cases the true acceptance angles are smaller than those defined by aperture f alone.

The integral of the detector efficiency over the interaction volume was carried out for various values of θ and the effective acceptance angle was found to change by less than 0.7% over our range of angles. Hence in analyzing the data we considered the detector acceptance to remain the same at all angles of the incident beam.

The divergence of the beam was determined by measuring the current in the collision cell as a function of the entrance-collimator position without changing the deflection voltages, and was less than 10^{-3} rad in all cases. The total angular resolution is a convolution of the acceptance angle of the detector with the divergence of the incident beam. We did not attempt deconvolution because,

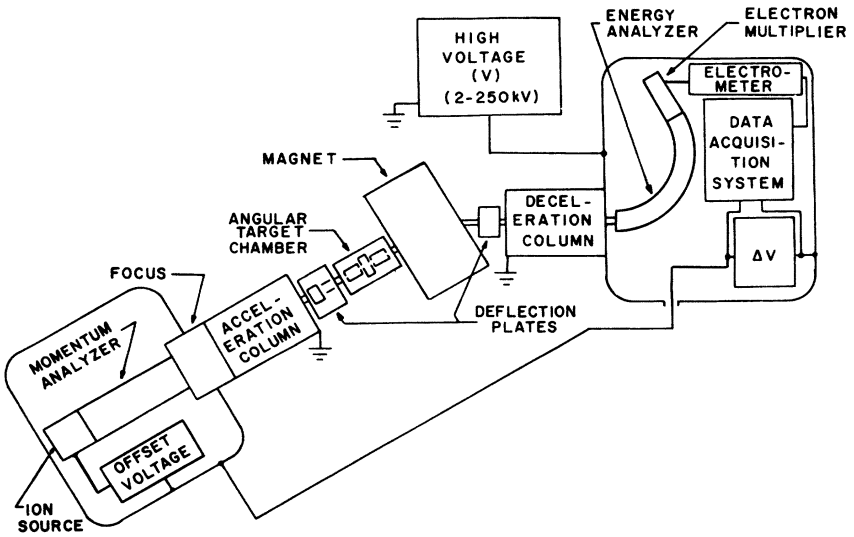

FIG. 1. Over-all schematic diagram of the apparatus.

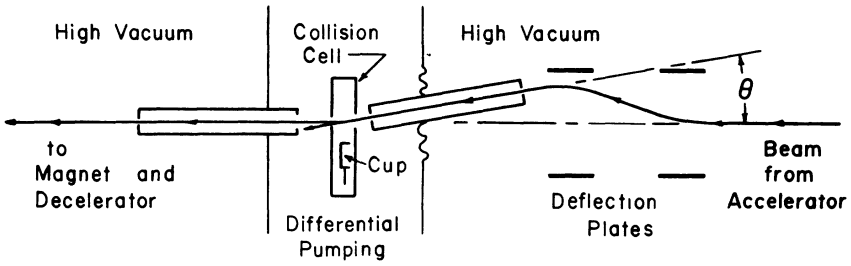

FIG. 2. Schematic diagram of the angular apparatus.

while we could measure the efficiency across the detector, we could not measure the angular distribution of the beam at all points in the collision cell. Nor could we estimate it from the geometry of the entrance collimator because the collimator slits do not determine the angular distribution, as evidenced from the fact that the maximum divergence which we measured was less than half the maximum divergence allowed by the collimator slits.

The convolution of the acceptance angle of the detector with the divergence of the incident beam was obtained by plotting $[I_{10}(\theta)]_{n=0}$, the current detected in the analyzer, as a function of incident beam angle with no gas in the collision cell. This measurement was consistent with the values of the angular acceptance and beam divergence obtained separately and hence was used to determine the angular resolution at each energy.

The target gas density at the center of the collision cell, n_0, was monitored by a differential pressure meter. A 3% correction due to effusion of the target gas through the entrance and exit apertures was made by calculating

$$(L)_{\text{eff}} = \frac{1}{n_0} \int n(x)\, dx$$

from basic kinetic theory.[13]

III. DATA

Typical Energy-Loss Spectra

A set of energy-loss spectra for He^+ incident on He is shown in Fig. 4. The features at $\theta = 0$ are similar to those of spectra obtained from the apparatus before angular measurement modifications were made.[2] The first peak, at 0-eV energy loss, corresponds to the initial beam or to particles which have been elastically scattered. The double peak between 19 and 22 eV is due to particles which have undergone discrete energy losses upon exciting the He($n=2$) states (at 19.815, 20.611, 20.959, and 21.213 eV). The peak at 40.8 eV is due to the excitation of the $He^+(n=2)$ states. Structure due to the He($n>2$) states was observed as an unresolved peak just before the ionization continuum. Because of the greatly reduced beam intensity which resulted from the angular-study modifications, we were not able to accurately measure the $He^+(n=3)$ excitation reported previously.[2] Peaks near 60 eV corresponding to autoionizing states and to simultaneous excitations of both the projectile and target were also below measurable intensities following these modifications. By looking carefully in the energy-loss region around 48 eV we did see the peak due to the $He^+(n=3)$ states at $\theta = 0$, but did not at $\theta \geq 2.4 \times 10^{-3}$ rad (c.m.).

Many of the qualitative features of He^+ +He angular scattering in our energy range are apparent from Fig. 4. The elastic peak (which accounts for more than 96% of the total detected current at this target density) decreases by more than two orders of magnitude within 2.4×10^{-3} rad (c.m.). Note that since the angular resolution at this energy is 2×10^{-3} rad (c.m.), the spectrum obtained at 2.4×10^{-3} rad includes contributions from par-

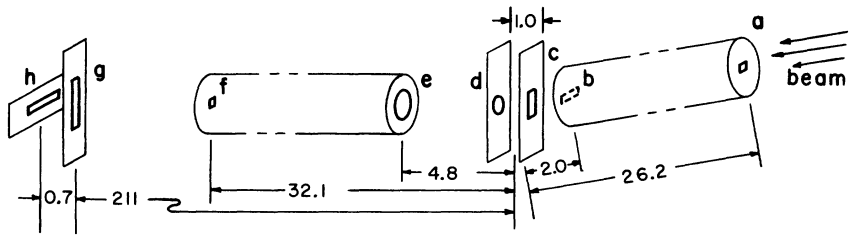

FIG. 3. Details of the collimators and defining apertures. *a* is a square 0.026× 0.026; *b* is a horizontal slit 0.15 × 0.028; *c* is a vertical slit 0.026× 0.18; *d* is a circular hole of diameter 0.065; *e* is a circular hole of diameter 0.15; *f* is a square 0.028× 0.028; *g* and *h* are vertical and horizontal slits 0.032× 2.5 which can be moved across the front of the decelerator. (All dimensions are given in centimeters.)

ticles which have been scattered by as little as 1.5×10^{-3} rad (c.m.). At larger angles the elastic peak is still the predominant feature, but it is of the same order of magnitude as the inelastic peaks. The shift in position of all the peaks agrees well with the expected energy loss due to pure elastic scattering.

The most striking feature of this set of spectra is the change in relative intensities of the He($n=2$) excitations. At $\theta=0$ the He($2\,^3S$) state accounts for more than 50% of the total He($n=2$) peak, while at $\theta\geq4.8\times10^{-3}$ rad it makes a very small contribution. This is similar to energy-loss spectra obtained at 0.6 keV by Lorents *et al.*,[14] who observe that initially the $2\,^3S$ contribution decreases with increasing angle. However they made their measurements at much larger angles ($\geq2\times10^{-2}$ rad, c.m.) and it is clear in their data that the contribution of the $2\,^3S$ does not remain low, but appears to oscillate as a function of angle. This feature might still hold true at our energies, but the total signal decreases so rapidly with increasing angle that we could not make measurements at larger angles.

The $He^+(n=2)$ excitation peak is also interesting because of its relatively broad angular dependence. In this particular set of data it has decreased by a factor of only 2×10^2 over the same angular range in which the He($n=2$) peak has decreased by a factor of 2×10^3 and the elastic peak had decreased by more than 2×10^4. This indicates that, at least in He^+-He collisions, the angular dependence of the excitation processes cannot be estimated from total scattering measurements which do not distinguish between the scattered ions.

Reduction of Data

The expression used to extract apparent differential cross sections from energy-loss data is given by

$$\frac{\Delta\sigma_p}{\Delta\Omega}(\theta)=\frac{1}{nL\Delta\Omega}\frac{[I_{1p}(\theta)]_f}{(I_{10})_f}\,, \tag{1}$$

where $[I_{1p}(\theta)]_f$ is the current under the appropriate peak in the energy-loss spectrum due to singly charged particles which have lost energy in the interaction p and have been scattered into the solid angle $\Delta\Omega$ at θ; $(I_{10})_f$ is the final current due to the elastic beam, integrated over all angles to obtain the total beam current. L is the length of the interaction region, n is the average target density, and $\Delta\Omega$ is the total solid angle subtended by the detector.

Equation (1) automatically incorporates effects of charge exchange and other inelastic processes. It is subject to the same limitations discussed in Ref. 2. A further limitation is the possibility of multiple collisions involving one energy-loss process and one or more elastic collisions. As a practical criterion we measured $\sigma_e(\theta>\frac{1}{2}\Delta\theta)$, the cross section for elastic scattering through angles greater than $\frac{1}{2}\Delta\theta$, where $\Delta\theta$ is the angular resolution of the apparatus in the vertical plane. With this definition for σ_e the approximation $e^{-\sigma_e nL}\approx1-\sigma_e nL$ was correct to within 1% at all our target densities, indicating that for practical purposes the single-collision criterion was met.

From sets of spectra taken at various angles, data were derived as pairs of current (integrated over the appropriate energy loss) versus angle for each process. Because of the rectangular nature of the beam collimators and analyzer apertures, each value of $[I_{1p}(\theta)]_f$ represents current scattered into a rectangular solid angle centered at θ. In order to calculate the total current, we divided the detection region into concentric rings of width $\Delta\theta$, with a central circle of diameter $\Delta\theta$. Then from the data we calculated the average

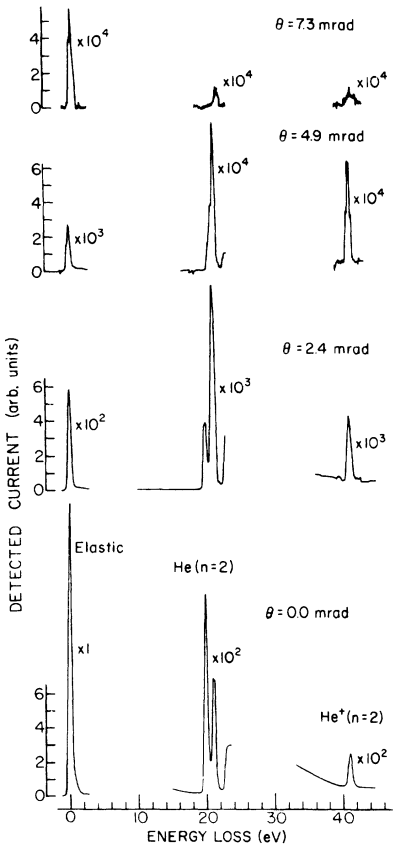

FIG. 4. Sample set of energy-loss spectra. The incident lab energy is 50 keV; the target thickness is 50 mtorr cm; the energy-loss resolution is 0.6 eV; the angular resolution is 2×10^{-3} rad (c.m.). All angles are given in units of 10^{-3} rad (c.m.).

current detected per solid angle, $J_p(\theta_i)$, at each ring. In terms of these current densities Eq. (1) becomes

$$\left\langle \frac{d\sigma_p}{d\Omega} \right\rangle_{av} = \frac{1}{nL} \frac{J_p(\theta_i)}{(I_{10})_f} \tag{2}$$

and can be interpreted to give the differential cross section, $(d\sigma_p/d\Omega)(\theta)$ averaged over the interval $\theta_i - \frac{1}{2}\Delta\theta$ to $\theta_i + \frac{1}{2}\Delta\theta$. The current scattered into each ring can be calculated by multiplying the current density of the ring times the solid angle subtended by the ring, and the total current can be found by adding up the currents in all the rings.

Average differential cross sections evaluated with Eq. (2) are given in Table I for all the energies we studied. (The cross sections and angles are given in center-of-mass coordinates, in which the angle is twice the lab angle and the differential cross section is $\frac{1}{4}$ the lab cross section.) The data were actually obtained at smaller angular spacings than indicated in the table, particularly close to $\theta = 0$, but are tabulated only at multiples of the angular resolution. The data have large uncertainty at large angles, where the signal-to-noise ratio was at the limit of the apparatus. The $He^+(n=2)$ data has the most uncertainty because it was generally the smallest peak measured.

Contributions of the He($n=2$) States

Further analysis of the He($n=2$) peak was carried out by a curve-fitting technique designed to estimate the contribution of each state to the total He($n=2$) excitation.[15] This involved superimposing the shape of the elastic peak at the expected location of each state in the energy-loss spectrum and, by a least-squares fit, finding the height of the peak at each location such that the sum of the four peaks best reproduced the data. Details concerning the limitations and uncertainties involved in applying this technique are included in Ref. 15. While this procedure gave quite reliable results for the He($2\,^3S$) state, there were often large fluctuations in the results for the other three states.

Differential cross sections calculated from the results of the curve-fitting technique are given in Table II for each He($n=2$) state. At 140 keV, and partly at some of the other high energies, the amount of scattering at nonzero angles was so small that the signal-to-noise ratio made the curve-fitting technique reliable only at angles close to $\theta = 0$; hence no results are given for 140 keV. The numbers in the table were obtained by multiplying the average fractional contribution of each state by the differential cross section given in Table I for the total He($n=2$) peak. The limits were obtained from the standard deviations in the cross section and the standard deviations in the fractions. Because of uncertainties in the curve-fitting technique the quoted errors are quite large although they are not unusually large for excitation cross-section measurements (see Ref. 1). If the cross sections for the $2\,^1S$, $2\,^3P$, and $2\,^1P$ states are added the fractional uncertainty in the sum is considerably reduced since the sum is clearly

TABLE I. Average differential cross sections (c.m.) for the three major peaks in the $He^+ + He$ energy-loss spectra.

θ(c.m.)[a] (10^{-3} rad)	Elastic peak[a] (cm^2/sr)	He($n=2$) peak[a] (cm^2/sr)	He^+($n=2$) peak[a] (cm^2/sr)
	Incident energy = 25 keV (lab)		
0.6 ± 0.6		$(8.8 \pm 1.3) \times 10^{-13}$	$(7.1 \pm 2.5) \times 10^{-14}$
2.4 ± 1.2	$(1.8 \pm 0.6) \times 10^{-12}$	$(2.1 \pm 0.5) \times 10^{-13}$	$(8.7 \pm 8.5) \times 10^{-15}$
4.9 ± 1.2	$(8.3 \pm 6.0) \times 10^{-14}$	$(5.8 \pm 2.3) \times 10^{-14}$	$(3.3 \pm 7.4) \times 10^{-15}$
7.3 ± 1.2	$(0.9 \pm 2.0) \times 10^{-14}$	$(2.8 \pm 1.1) \times 10^{-14}$	$(1.0 \pm 6.0) \times 10^{-15}$
	Incident energy = 30 keV (lab)		
0.4 ± 0.4		$(1.4 \pm 0.1) \times 10^{-12}$	$(1.0 \pm 0.2) \times 10^{-13}$
1.5 ± 0.7	$(3.0 \pm 1.1) \times 10^{-11}$	$(6.8 \pm 1.1) \times 10^{-13}$	$(4.8 \pm 2.0) \times 10^{-14}$
2.9 ± 0.7	$(9.8 \pm 2.0) \times 10^{-13}$	$(2.2 \pm 0.4) \times 10^{-13}$	$(1.6 \pm 0.9) \times 10^{-14}$
4.4 ± 0.7	$(1.0 \pm 0.3) \times 10^{-13}$	$(6.3 \pm 1.2) \times 10^{-14}$	$(6.5 \pm 8.0) \times 10^{-15}$
5.8 ± 0.7	$(1.6 \pm 1.0) \times 10^{-14}$	$(2.1 \pm 0.5) \times 10^{-14}$	$(2.9 \pm 6.0) \times 10^{-15}$
7.3 ± 0.7	$(2.8 \pm 5.0) \times 10^{-14}$	$(7.9 \pm 4.0) \times 10^{-15}$	$(1.7 \pm 5.0) \times 10^{-15}$
	Incident energy = 40 keV (lab)		
0.6 ± 0.6		$(1.8 \pm 0.6) \times 10^{-12}$	$(9.3 \pm 2.5) \times 10^{-14}$
2.4 ± 1.2	$(7.3 \pm 3.5) \times 10^{-13}$	$(2.3 \pm 0.5) \times 10^{-12}$	$(2.6 \pm 1.1) \times 10^{-14}$
4.9 ± 1.2	$(1.6 \pm 0.9) \times 10^{-14}$	$(2.0 \pm 1.0) \times 10^{-14}$	$(4.6 \pm 2.5) \times 10^{-15}$
7.3 ± 1.2	$(3.5 \pm 3.0) \times 10^{-15}$	$(4.4 \pm 2.4) \times 10^{-15}$	$(1.7 \pm 1.2) \times 10^{-15}$
	Incident energy = 50 keV (lab)		
0.5 ± 0.5		$(2.0 \pm 0.2) \times 10^{-12}$	$(2.3 \pm 0.4) \times 10^{-13}$
1.9 ± 1.0	$(1.4 \pm 0.6) \times 10^{-12}$	$(2.9 \pm 0.7) \times 10^{-13}$	$(5.6 \pm 1.7) \times 10^{-14}$
3.9 ± 1.0	$(4.7 \pm 1.2) \times 10^{-14}$	$(2.3 \pm 0.7) \times 10^{-14}$	$(1.1 \pm 0.4) \times 10^{-14}$
5.8 ± 1.0	$(8.2 \pm 4.0) \times 10^{-15}$	$(3.1 \pm 1.2) \times 10^{-15}$	$(2.4 \pm 1.2) \times 10^{-15}$
	Incident energy = 70 keV (lab)		
0.5 ± 0.5		$(3.0 \pm 0.6) \times 10^{-12}$	$(6.7 \pm 2.7) \times 10^{-13}$
1.9 ± 1.0	$(1.5 \pm 1.1) \times 10^{-12}$	$(1.7 \pm 1.1) \times 10^{-13}$	$(2.7 \pm 2.0) \times 10^{-14}$
3.9 ± 1.0	$(2.2 \pm 1.9) \times 10^{-14}$	$(4.8 \pm 5.0) \times 10^{-15}$	$(4.3 \pm 3.9) \times 10^{-15}$
5.8 ± 1.0	$(5.4 \pm 6.0) \times 10^{-15}$	$(1.0 \pm 2.0) \times 10^{-15}$	$(2.6 \pm 2.0) \times 10^{-15}$
	Incident energy = 80 keV (lab)		
0.4 ± 0.4		$(2.4 \pm 0.4) \times 10^{-12}$	$(5.8 \pm 0.9) \times 10^{-13}$
1.7 ± 0.8	$(1.4 \pm 0.6) \times 10^{-12}$	$(2.6 \pm 0.9) \times 10^{-13}$	$(4.6 \pm 2.4) \times 10^{-14}$
3.4 ± 0.8	$(3.4 \pm 1.8) \times 10^{-14}$	$(1.3 \pm 0.8) \times 10^{-14}$	$(6.9 \pm 5.2) \times 10^{-15}$
5.1 ± 0.8	$(1.3 \pm 0.9) \times 10^{-14}$	$(1.8 \pm 1.3) \times 10^{-15}$	$(3.0 \pm 2.8) \times 10^{-15}$
	Incident energy = 100 keV (lab)		
0.4 ± 0.4		$(2.6 \pm 0.3) \times 10^{-12}$	$(6.5 \pm 1.0) \times 10^{-13}$
1.7 ± 0.8	$(1.5 \pm 0.7) \times 10^{-12}$	$(1.9 \pm 0.5) \times 10^{-13}$	$(3.6 \pm 1.3) \times 10^{-14}$
3.4 ± 0.8	$(1.4 \pm 0.4) \times 10^{-14}$	$(5.1 \pm 1.3) \times 10^{-15}$	$(3.1 \pm 1.4) \times 10^{-15}$
5.1 ± 0.8	$(4.6 \pm 3.0) \times 10^{-15}$	$(7.8 \pm 5.0) \times 10^{-16}$	$(1.1 \pm 0.6) \times 10^{-15}$
	Incident energy = 120 keV (lab)		
0.3 ± 0.3		$(4.4 \pm 0.7) \times 10^{-12}$	$(9.8 \pm 1.0) \times 10^{-13}$
1.2 ± 0.6	$(4.4 \pm 2.5) \times 10^{-12}$	$(2.3 \pm 0.6) \times 10^{-13}$	$(7.8 \pm 3.5) \times 10^{-14}$
2.4 ± 0.6	$(5.1 \pm 4.0) \times 10^{-14}$	$(2.1 \pm 1.0) \times 10^{-14}$	$(4.1 \pm 3.0) \times 10^{-15}$
	Incident energy = 140 keV (lab)		
0.2 ± 0.2		$(9.6 \pm 0.9) \times 10^{-12}$	$(2.0 \pm 0.2) \times 10^{-12}$
0.8 ± 0.4	$(1.3 \pm 0.9) \times 10^{-11}$	$(5.7 \pm 2.0) \times 10^{-13}$	$(1.2 \pm 1.1) \times 10^{-13}$
1.7 ± 0.4	$(1.0 \pm 1.3) \times 10^{-13}$	$(2.2 \pm 1.0) \times 10^{-14}$	$(2.4 \pm 5.0) \times 10^{-15}$

[a] Limits on the angle denote the angular resolution; limits on the differential cross sections denote the standard deviations in the data.

resolved. It was felt that the additional information obtained warranted the use of the curve-fitting technique in spite of the increased uncertanties.

Total Excitation Cross Sections

The total cross section for each process can be obtained by integrating the differential cross sections given in Tables I and II. This is not the ideal method for obtaining total cross sections, since it depends strongly on precise evaluation of the angular resolution of the apparatus and since the integration should include all possible scattering angles. Nevertheless, our total cross sections calculated in this manner probably have systematic errors of less than 35% in most cases (see Sec. IV).

Figure 5 shows plots of the total excitation cross

TABLE II. Average differential cross sections (c.m.) for the four states contributing to the He($n=2$) peak.

θ(c.m.) [a] (10^{-3} rad)	He(2^3S) [a] (cm^2/sr)	He(2^1S) [a] (cm^2/sr)	He(2^3P) [a] (cm^2/sr)	He(2^1P) [a] (cm^2/sr)
		Incident energy = 25 keV (lab)		
0.6 ± 0.6	$(2.5\pm0.8)\times10^{-13}$	$(0.4\pm0.5)\times10^{-13}$	$(4.2\pm1.6)\times10^{-13}$	$(1.8\pm1.0)\times10^{-13}$
2.4 ± 1.2	$(2.5\pm1.9)\times10^{-14}$	$(4.6\pm3.2)\times10^{-14}$	$(4.0\pm4.8)\times10^{-14}$	$(9.5\pm5.6)\times10^{-14}$
4.9 ± 1.2	$(0.6\pm0.7)\times10^{-14}$	$(1.2\pm1.2)\times10^{-14}$	$(0.6\pm1.8)\times10^{-14}$	$(3.5\pm3.3)\times10^{-14}$
7.3 ± 1.2	$(0.2\pm0.6)\times10^{-14}$	$(0.6\pm0.9)\times10^{-14}$	$(0.6\pm1.8)\times10^{-14}$	$(1.5\pm2.3)\times10^{-14}$
		Incident energy = 30 keV (lab)		
0.4 ± 0.4	$(4.3\pm0.8)\times10^{-13}$	$(1.3\pm0.7)\times10^{-13}$	$(7.7\pm2.0)\times10^{-13}$	$(0.7\pm1.0)\times10^{-13}$
1.5 ± 0.7	$(1.6\pm0.6)\times10^{-13}$	$(0.6\pm0.5)\times10^{-13}$	$(4.1\pm1.6)\times10^{-13}$	$(0.5\pm0.9)\times10^{-13}$
2.9 ± 0.7	$(0.2\pm0.1)\times10^{-13}$	$(0.3\pm0.2)\times10^{-13}$	$(0.6\pm0.3)\times10^{-13}$	$(1.1\pm0.5)\times10^{-13}$
4.4 ± 0.7	$(0.5\pm0.4)\times10^{-14}$	$(1.5\pm1.0)\times10^{-14}$	$(0.6\pm0.6)\times10^{-14}$	$(3.7\pm1.8)\times10^{-14}$
5.9 ± 0.7	$(0.2\pm0.2)\times10^{-14}$	$(0.5\pm0.4)\times10^{-14}$	$(0.1\pm0.3)\times10^{-14}$	$(1.3\pm0.8)\times10^{-14}$
7.3 ± 0.7	$(0.8\pm1.3)\times10^{-15}$	$(1.3\pm1.7)\times10^{-15}$	$(0.3\pm1.9)\times10^{-15}$	$(5.3\pm5.6)\times10^{-15}$
		Incident energy = 40 keV (lab)		
0.6 ± 0.6	$(8.8\pm3.7)\times10^{-13}$	$(5.4\pm9.0)\times10^{-14}$	$(7.4\pm4.6)\times10^{-13}$	$(1.8\pm2.3)\times10^{-13}$
2.4 ± 1.2	$(3.9\pm3.6)\times10^{-14}$	$(3.9\pm3.5)\times10^{-14}$	$(5.3\pm5.3)\times10^{-14}$	$(9.7\pm7.7)\times10^{-14}$
4.9 ± 1.2	$(2.2\pm5.0)\times10^{-15}$	$(3.8\pm6.7)\times10^{-15}$	$(3.6\pm9.9)\times10^{-15}$	$(1.0\pm1.1)\times10^{-14}$
		Incident energy = 50 keV (lab)		
0.5 ± 0.5	$(12\pm3)\times10^{-13}$	$(0.8\pm1.4)\times10^{-13}$	$(5.6\pm2.1)\times10^{-13}$	$(2.4\pm2.0)\times10^{-13}$
1.9 ± 1.0	$(8.1\pm4.1)\times10^{-14}$	$(4.9\pm5.9)\times10^{-14}$	$(6.7\pm8.1)\times10^{-14}$	$(9.3\pm9.1)\times10^{-14}$
3.9 ± 1.0	$(2.1\pm2.1)\times10^{-15}$	$(4.6\pm5.6)\times10^{-15}$	$(4.6\pm6.8)\times10^{-15}$	$(12\pm10)\times10^{-15}$
5.8 ± 1.0	$(0.2\pm0.3)\times10^{-15}$	$(0.6\pm0.9)\times10^{-15}$	$(0.5\pm1.3)\times10^{-15}$	$(2.0\pm2.3)\times10^{-15}$
		Incident energy = 70 keV (lab)		
0.5 ± 0.5	$(1.7\pm0.5)\times10^{-12}$	$(0.2\pm0.1)\times10^{-12}$	$(0.6\pm0.4)\times10^{-12}$	$(0.5\pm0.4)\times10^{-12}$
1.9 ± 1.0	$(6.3\pm6.3)\times10^{-14}$	$(0.7\pm3.8)\times10^{-14}$	$(6.8\pm8.6)\times10^{-14}$	$(2.9\pm4.4)\times10^{-14}$
3.9 ± 1.0	$(0.6\pm1.4)\times10^{-15}$	$(1.4\pm4.9)\times10^{-15}$	$(1.0\pm3.0)\times10^{-15}$	$(1.6\pm5.4)\times10^{-15}$
		Incident energy = 80 keV (lab)		
0.4 ± 0.4	$(13\pm3)\times10^{-13}$	$(3.4\pm2.2)\times10^{-13}$	$(3.4\pm2.8)\times10^{-13}$	$(4.8\pm2.8)\times10^{-13}$
1.7 ± 0.8	$(9.9\pm5.9)\times10^{-14}$	$(2.3\pm3.3)\times10^{-14}$	$(8.3\pm8.1)\times10^{-14}$	$(5.7\pm6.2)\times10^{-14}$
3.4 ± 0.8	$(2.9\pm4.3)\times10^{-15}$	$(0.9\pm2.7)\times10^{-15}$	$(3.9\pm7.6)\times10^{-15}$	$(6\pm12)\times10^{-15}$
		Incident energy = 100 keV (lab)		
0.4 ± 0.4	$(11\pm2)\times10^{-13}$	$(3.9\pm2.2)\times10^{-13}$	$(4.4\pm2.5)\times10^{-13}$	$(7.0\pm3.4)\times10^{-13}$
1.7 ± 0.8	$(7.8\pm4.0)\times10^{-14}$	$(1.3\pm1.6)\times10^{-14}$	$(5.7\pm4.4)\times10^{-14}$	$(4.8\pm3.2)\times10^{-14}$
3.4 ± 0.8	$(1.6\pm1.1)\times10^{-15}$	$(0.9\pm1.0)\times10^{-15}$	$(1.5\pm2.4)\times10^{-15}$	$(1.0\pm2.0)\times10^{-15}$
		Incident energy = 120 keV (lab)		
0.3 ± 0.3	$(1.2\pm0.3)\times10^{-12}$	$(1.1\pm0.5)\times10^{-12}$	$(0.2\pm0.4)\times10^{-12}$	$(1.9\pm0.8)\times10^{-12}$
1.2 ± 0.6	$(8.5\pm4.0)\times10^{-14}$	$(3.9\pm2.5)\times10^{-14}$	$(3.9\pm3.9)\times10^{-14}$	$(7.4\pm7.7)\times10^{-14}$

[a] Limits on the angles denote the angular resolution; limits on the differential cross sections denote the standard deviations in the data.

sections for the individual He($n=2$) states. Figure 6 gives plots for the He($n=2$) peak and the He^+ ($n=2$) peak. The vertical bar in each case is the standard deviation in the data, obtained by integrating the deviations in the differential cross sections at all the angles; the total error can be estimated from these deviations and the systematic errors discussed in Sec. IV. Because the angular resolution depends strongly on the incident energy, the effects of the systematic errors due to uncertainty in the angular resolution also depend on the energy; i.e., at one energy our measurements may be too high because of these errors and at another energy they may be too low. Hence this uncertainty may affect the shapes of the total cross-section curves as well as the absolute magnitudes.

Also shown are impact-parameter calculations of Sural *et al.*[16] for direct excitation of the He (2^3S) and He(2^1S) states and the measurement of Lorents *et al.*[14] at 0.6 keV for the He(2^3S) state. The value of Lorents *et al.* does not appear to fit on a smooth extrapolation of our data. The apparent discrepancy may be due to a change in the excitation mechanism, causing the He(2^3S) state to dominate again at lower energies, or it may be due to systematic errors in the measurements which cause our values to be too low and/or their value too high. Of course there may not be a real discrepancy between the measurements, since the values agree within the combined error bars and the apparent shape in our data may be misleading.

In the previous measurements of Schoonover and Park[2,3] only forward-scattered components were detected and the results were given as total cross sections by assuming that scattering out of the angular acceptance of the apparatus was negligible, whereas the present experiments indicate that angular scattering is significant. Most of the previous results are nevertheless within the error bars at incident energies above 40 keV; at

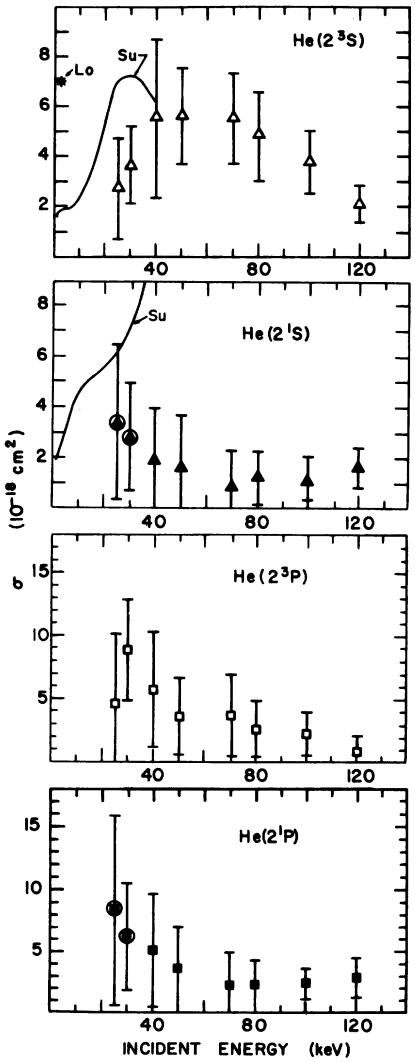

FIG. 5. Total cross sections for excitation of the He (2^3S), He(2^1S), He(2^3P), and He(2^1P) states. The starred point is the measurement of Lorents *et al.* (Ref. 14); the solid curves are the calculation of Sural *et al.* (Ref. 16), and the triangles are the present data. The circled points may be too low due to scattering outside of our angular range (see Sec. IV).

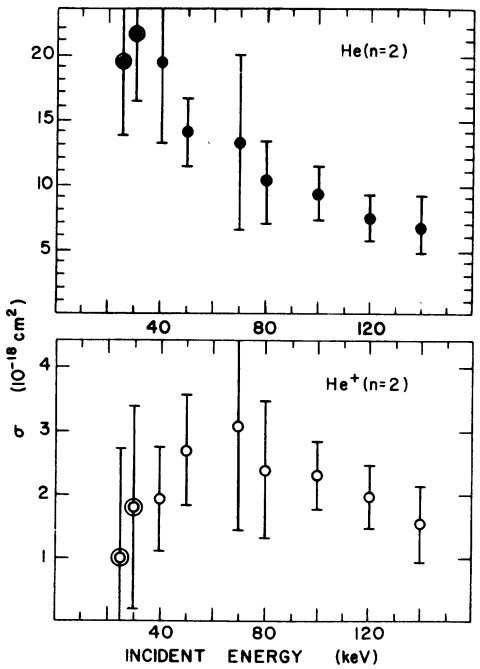

FIG. 6. Total cross sections for the He($n=2$) and He^+ ($n=2$) excitation peaks. The circled points may be too low due to scattering outside of our angular range (see Sec. IV).

20 and 30 keV they may have been in error by a factor of 5 or more. If the present measurements are analyzed in the same manner as Schoonover's, the results agree very well with his measurements, although the geometries of both the scattering chamber and the ion source are quite different.

IV. ERROR ANALYSIS

The target gas pressure was monitored by an MKS Baratron[17] type 77H capacitance manometer with a type 77H1 pressure head that had recently been recalibrated by the manufacturer. From the manufacturer's literature we estimate that at our pressures (20–100 mtorr) the total systematic error in the pressure measurements was less than 5%. Random error due to fluctuations in pressure was reduced to less than 0.5% by recording the pressure on punched tape simultaneously with the current–energy-loss data and correcting each datum point by the actual pressure recorded with the point.

The largest source of systematic error, and the one most difficult to analyze, is the determination of the angular resolution of the apparatus. In evaluating the current densities $J_p(\theta_i)$ we assumed that all of the current we detected had been scattered through well-defined angles, whereas in fact the angular resolution is not so sharply defined. This error tends to cancel out in determining the magnitude of the averaged measurements since the acceptance angle occurs in both $J_p(\theta_i)$ and in the total elastic current $(I_{10})_f$. By assuming various values of the angular resolution [other than those obtained from measurements of $I_{10}(\theta)$ with no gas in the collision cell] we were able to estimate the effect of errors in the angular resolution. A large variation in the rectangular solid angle used in the calculations of $J_p(\theta_i)$ produced a much smaller effect in the differential cross sections. Furthermore, the variations had even less effect on the shape of $\langle d\sigma/d\Omega\rangle_{av}$.

We estimate that the total systematic error in the absolute magnitude of our measurements due to errors in n, L, and the angular resolution is less than 35%. The observed shape of the differential cross section may be broader than the true shape because we measure a weighted average over a relatively wide angular region.

Some of the total cross sections at 25 and 30 keV are too low if scattering outside of our largest angles is not negligible. We did not correct for this effect since our maximum angles were dictated by the signal-to-noise ratio and any extrapolation would be based on our least-reliable measurements. Hence the data given in Figs. 5 and 6 were not corrected for scattering outside our range of angles. Using possible extrapolations of the differential cross sections we estimate that at 25 keV the contribution from large angles to the total He($n=2$) cross section may be 10–100% of the value given in Fig. 6, while at 30 keV it is probably no more than 10%. This affects primarily the He($2\,^1P$) and He($2\,^1S$) states, since the other two states appear to decrease rapidly with increasing angle at these energies. The same correction appears to be necessary for the $He^+(n=2)$ peak, for which we estimate that the contribution from larger angles may add 20–100% at 25 keV and 10–30% at 30 keV.

V. DISCUSSION

Comparison of Total Cross Sections

The closest experimental values in this energy range with which we can compare are measurements of Gilbody *et al.*,[18] who report the total cross section for electron capture into the metastable states of He (i.e., the $2\,^1S$, $2\,^3S$, and $2\,^3P$ states and some states with $n>2$) with estimates of the contribution from states with $n>2$. Their results agree with the sum of our total cross sections for direct excitation of the He($2\,^1S$, $2\,^3S$, and $2\,^3P$) states at energies up to 40 keV. Above 50 keV their results are higher. Although the theoretical calculations of Sural *et al.*[16] do not give good agreement with our data, they do show that the total cross sections for electron capture into the He($2\,^1S$ and $2\,^3S$) states are nearly identical to the cross sections for direct excitation into those states at energies up to 30 keV. At higher energies they obtain higher cross sections for electron-capture excitation than for direct excitation. The agreement of our work with that of Gilbody *et al.* is consistent with these features.

The difference between our total cross sections for the He($2\,^3S$) and He($2\,^1S$) states and the calculations of Sural *et al.* (see Fig. 5) is difficult to explain. They indicate that at 40 keV the He($2\,^1S$) excitation cross section is larger than the He($2\,^3S$) cross section, while our data indicate that the He($2\,^3S$) state is the dominant feature from 40 to 100 keV. Their results for electron capture into the He($2\,^3S$ and $2\,^1S$) states agree well with measurements of Gilbody *et al.*[18] on electron capture into the He($2\,^3S$, $2\,^1S$, and $2\,^3P$) states, indicating that either the contribution of the He($2\,^3P$) state is negligible in electron-capture processes, or else the calculations of Sural *et al.* are too high. Furthermore, Sural *et al.* give plots of excitation probabilities versus impact parameter which indicate that at large impact parameters the probability of exciting the He($2\,^1S$) state is more

than twice as large (at 40 keV) as the probability of exciting the He(2^3S) state. This is contrary to our observations, since sets of spectra such as that shown in Fig. 4 indicate that at small angles (large impact parameters) the contribution of the He(2^3S) state is almost as large as the contribution of the He(2^1S, 2^3P, and 2^1P) states together. In fact, the general features of the excitation-probability versus impact-parameter plots given by Sural *et al.* disagree with the results of our curve-fitting process at any energy.

Discussion of Angular Dependence

Figure 7 shows smoothed-out plots of the results of our curve-fitting process for finding the contribution of each He($n=2$) state to the total He($n=2$) peak. The data are given as fractional contributions versus the reduced angle $E\theta$ in order to illustrate the relative behavior of each state. While there are large uncertainties in some of the contributions, the trends illustrated in the figures were generally observed in all our data:

a. He(2^3S). The 2^3S state definitely dominates the He($n=2$) structure at energies from 40 to 100 keV. At all energies below 100 keV its fractional contribution decreases sharply with angle. At 100 keV it contributes more than 30% to the He ($n=2$) peak at all angles, while at 120 and 140 keV the fractional contribution of the 2^3S state actually increases with increasing angle.

b. He(2^1P). The 2^1P state could almost be considered the complement of the 2^3S state, since its contribution is sharply increasing with angle at every energy where the 2^3S contribution decreases with angle.

c. He(2^3P). The 2^3P state exhibits similar angular dependence to that of the 2^3S except that the change in shape occurs at lower energies. While the 2^3S contribution did not flatten out until 100 keV, the contribution of the 2^3P is relatively uniform at 50 keV and is definitely increasing with angle at higher energies.

d. He(2^1S). The 2^1S state never contributes more than 25%, so there is more uncertainty in its shape because the fitting technique is less reliable in finding small contributions. Nevertheless the shape of the 25- and 50-keV curves is typical of all our observations in that energy

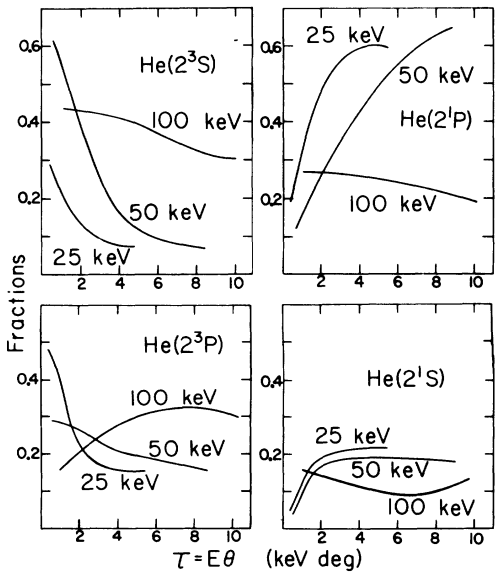

FIG. 7. Fractional contributions of the He(2^3S), He (2^1P), He(2^3P), and He(2^1S) states to the He($n=2$) excitation peak. The curves are displayed to illustrate trends observed in the data. Actual fractions if desired should be obtained from Table II.

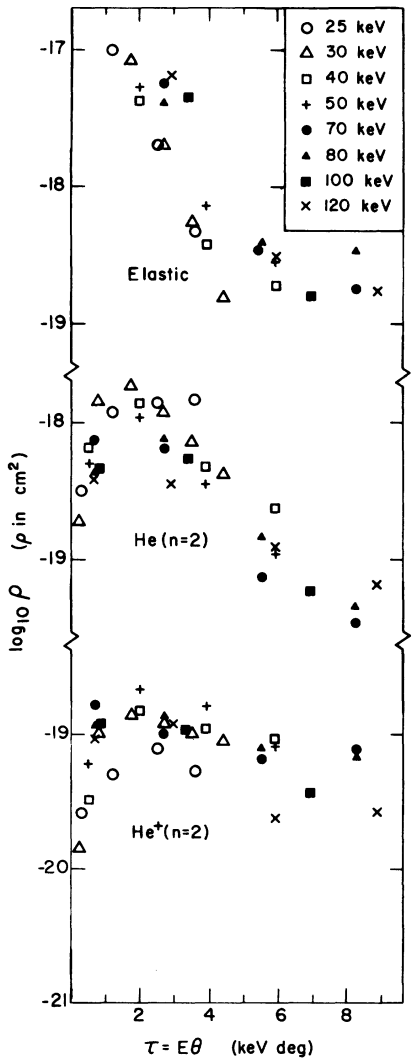

FIG. 8. Plots of ρ vs τ for the elastic peak, the He($n=2$) excitation peak and the He^+($n=2$) excitation peak.

range; i.e., the contribution is less than 8% at $\theta = 0$ and increases to approximately 20% at larger angles. There appears to be an abrupt change at 70 keV, above which the 2^1S contribution is 15 to 20% at $\theta = 0$.

By a straightforward application of the electron-promotion model,[19] Barat *et al.*[20] constructed a correlation diagram for the $He^+ + He$ system. According to this diagram, the He(2^3P and 2^1P) states and the $He^+(2P)$ states may be excited by rotational or radial coupling, but the He(2^3S and 2^1S) states may be excited only by radial coupling. McCarroll and Piacentini[21] made detailed calculations on the effects of rotational coupling at energies of 0.6–3.0 keV and, while they do not explain all of our data, their predictions are consistent with some of our observations at low energies. The main feature of their discussion is that radial coupling is expected to dominate at small values of $\tau = E\theta$ while rotational coupling should be dominant for $\tau \geq 3$ keV deg. We cannot separate the $He^+(n=2)$ states, but the relatively wide angular dependence which we observed in the $He^+(n=2)$ peak and our failure to see any excitation of the $He^+(n=3)$ states at nonzero angles are consistent with their prediction. The dramatic increase with angle (at energies below 80 keV) in the fractional contribution of the He(2^1P) state and the decrease in the contribution of the He(2^3S) state (see Fig. 7) are also in good agreement with their prediction. An apparent discrepancy is in the angular dependence of the He(2^3P) state and the He(2^1S) state, which appear to differ markedly from the He(2^1P) and the He(2^3S) states, respectively. The electron-promotion model[19] does not distinguish between singlet and triplet states. McCarroll and Piacentini include separate terms for the He(2^3P) and the He(2^1P) states in their calculations, but their results are given for the two states together. They do point out that the He($2P$) states can also be excited by radial coupling, but that this effect should reach a maximum at $\tau \approx 0.6$ keV deg. It may be that the radial coupling accounts primarily for the large He(2^3P) excitation which we observed at small values of $E\theta$, while the rotational transitions are associated primarily with the He(2^1P) state and the $He^+(n=2)$ excitations. This interpretation implies that radial coupling is not as strong for singlet excitations as for triplet excitations and hence would explain why the He(2^1S) contributions is consistently low.

Plots of ρ vs τ, where $\rho = \theta \sin(\theta)(d\sigma/d\Omega)$ and $\tau = E\theta$, permit comparison of data obtained at different impact energies. Figure 8 shows such plots for our elastic, He($n=2$) and $He^+(n=2)$ data. In spite of the large energy range, common curves could be drawn within the error bars (not shown) of most of the points.

From the data of Barat *et al.*[20] and Lorents and Aberth[22] we calculated ρ vs τ curves to compare with our data. The values of ρ vs τ for the elastic-scattering data of Lorents and Aberth are generally higher than our values shown in Fig. 8, but several of the points are well within our error bars. The data of Barat *et al.* were given in relative units, so that only the shape could be compared with our data. For the elastic peak the shape of ρ vs τ calculated from their data, as well as from the data of Lorents and Aberth, is similar to the shape of our plots given in Fig. 8 if one averages out the oscillations which they observe. This agreement observed between the various sets of data for the elastic peak was not observed for the inelastic peaks. For the inelastic processes the values of ρ calculated from the data of Barat *et al.* at 2 and 3 keV reach maxima at 5 to 7 keV deg for the He($n=2$) peak and at 7 to 11 keV deg for the $He^+(n=2)$ peak, while our data reach maxima at approximately 2 keV deg. Several explanations may be given for this difference in shape. The excitation mechanism may have changed or it may include velocity dependent terms. It is also possible that the curves shown in Figs. 7 and 8 could display additional structure at larger values of $E\theta$.

The measurement of energy-loss spectra as a function of scattering angle provides a great deal of information about the dominate excitation mechanisms. The technique also provides straightforward methods for obtaining absolute measurements although it is still subject to the difficulties associated with small angle-scattering measurements. The very nature of our method requires a relatively large total detected current, hence limiting somewhat the range of scattering angles. Nevertheless, the range of differential-cross-section values covers four orders of magnitude. In spite of the difficulties, we have attempted to give the absolute magnitudes as well as the curve shapes in the hope that the results will be useful in comparison to theoretical calculations.

*Work supported through a grant from the National Science Foundation.

†Current address: Wayne State University, Detroit, Mich. 48202.

[1]E. W. Thomas, *Excitation in Heavy Particle Collisions* (Wiley, New York, 1972).

[2]D. R. Schoonover and J. T. Park, Phys. Rev. A 3, 228 (1971).

[3]D. R. Schoonover and J. T. Park, *Seventh International Conference on the Physics of Electronic and Atomic Collisions: Abstracts of Papers* (North-Holland, Amsterdam, 1971), p. 839.

[4]J. T. Park and F. D. Schowengerdt, Rev. Sci. Instrum. 40, 753 (1969).

[5]J. T. Park and F. D. Schowengerdt, Phys. Rev. 185, 152 (1969).

[6]G. W. York, J. T. Park, J. J. Miskinis, D. H. Crandall, and V. Pol, Rev. Sci. Instrum. 43, 230 (1972).

[7]E. B. Jordan and R. B. Brode, Phys. Rev. 43, 112 (1933).

[8]P. R. Jones, F. P. Ziemba, H. A. Moses, and E. Everhart, Phys. Rev. 113, 182 (1959).

[9]E. A. Silverstein, Nucl. Instr. Methods 4, 53 (1959).

[10]G. E. Chamberlain, S. R. Mielczarek, and C. E. Kuyatt, Phys. Rev. A 2, 1905 (1970).

[11]L. G. Filippenko, Zh. Tekh. Fiz. 30, 57 (1960).

[12]M. J. Van der Wiel, Physica (Utr.) 49, 411 (1970).

[13]N. F. Ramsey, *Molecular Beams* (Oxford U. P., London, 1956), Chap. II.

[14]D. C. Lorents, W. Aberth, and V. W. Hesterman, Phys. Rev. Lett. 17, 849 (1966).

[15]G. W. York, J. T. Park, V. Pol, and D. H. Crandall, Phys. Rev. A 6, 1497 (1972).

[16]D. P. Sural, S. C. Mukherjee, and N. C. Sil, Phys. Rev. 164, 156 (1967).

[17]MKS Instruments, Inc., Burlington, Mass.

[18]H. B. Gilbody, K. F. Dunn, R. Browning, and C. J. Latimer, J. Phys. B 4, 800 (1971).

[19]M. Barat and W. Lichten, Phys. Rev. A 6, 211 (1972).

[20]M. Barat, D. Dhuicq, R. Francois, R. McCarroll, R. D. Piacentini, and A. Salin, J. Phys. B 5, 1343 (1972).

[21]R. McCarroll and R. D. Piacentini, J. Phys. B 4, 1026 (1971).

[22]D. C. Lorents and W. Aberth, Phys. Rev. 139, A1017 (1965).